Integrated Magnetics Design for a Full-Bridge Phase-Shifted Converter

Yu-Chen Liu[1], Chen Chen[2], Shu-Yi Lin[2], Cheng-You Xiao[2], Katherine A. Kim[3], Yao-Ching Hsieh[2], and Huang-Jen Chiu[2]

[1]Department of Electrical Engineering
National Ilan University
Yilan, Taiwan, Taiwan

[2]Department of Electronic and Computer Engineering,
National Taiwan University of Science and Technology
Taipei, Taiwan

[3]School of Electrical and Computer Engineering
Ulsan National Institute of Science and Technology
Ulsan, South Korea

***Abstract*—Full-bridge phase-shifted converters sometimes add external resonant inductors to achieve zero-voltage switching during light load conditions. The magnetic components in the circuit include a resonant inductor, transformer, and output inductor. These magnetic components occupy a sizable portion of the circuit volume, which results in low power density. To achieve higher power density, this paper analyzes the magnetic integration of these three magnetic components into one core. This analysis derives the flux density and output ripple current by calculating the dc-ac flux and equivalent output inductance during operation intervals. The resonant inductor in the traditional full-bridge phase-shifted converter is replaced by adjusting the distance between primary-side winding and secondary-side winding. Finally, the prototype of a 500-W full-bridge phase-shifted converter which operates with 380-V input voltage and 12-V output voltage is implemented using integrated magnetic technology.**

Keywords—*full-bridge phase-shifted converter; magnetic integration; zero voltage switching*

I. INTRODUCTION

To meet the needs of modern products, many switch-mode power supplies require high power density and low profile. One of the ways to decrease the volume of a circuit is to increase the switching frequency. However, the efficiency will decrease due to high switching loss. This problem can be solved using soft switching techniques, such as zero voltage switching (ZVS) or zero current switching (ZCS) [1, 2].

Full-bridge phase-shifted converters [1-5] are widely used at medium and high power. This topology sometimes uses an external resonant inductor, output inductor and switching's stray capacitor to allow the primary-side switching to achieve zero voltage switching (ZVS). The trade-off is that the magnetic components increase the volume and decrease the converter power density. To solve the low power density problem, some papers use an integrated magnetic concept [6-10] to integrate many magnetic components into one core. This work integrates the magnetics in a full-bridge phase-shifted converter with a center-tapped topology in order to increase power density.

Previous work used a magnetic integration technique for a current-doubler topology of a full-bridge phase-shifted converter [11-17]. Work in [18] investigates the full-bridge phase-shifted converter, but with a different integration technique. Work in [19] uses a magnetic integration applied to a non-phase-shifted full-bridge converter. This paper utilizes a similar approach as in [19] to integrate all the magnetic components into one core for a phase-shifted full-bridge topology. By analyzing the dc-ac flux and equivalent output inductance during each operation interval, the core flux density and output ripple current can be derived. The resonant inductor is replaced by adjusting the distance between primary- and secondary-side winding. Thus, the resonant inductor, transformer, and output inductor in the full-bridge phase-shifted converter can be integrated into one core. Its performance is verified using a 500-W experimental prototype.

II. INTEGRATED MAGNETIC STRUCTURE

Fig. 1 shows the topology of center-tapped full-bridge phase-shifted converter. The magnetic component in the circuit includes resonant inductor, transformer and output inductor.

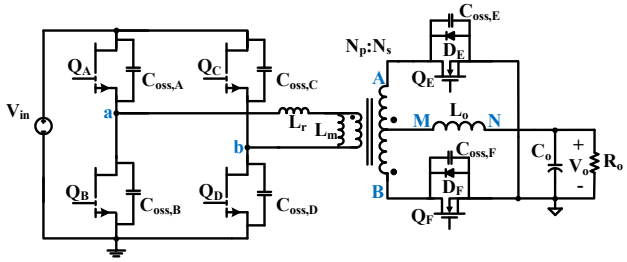

Fig. 1. Center-tapped full-bridge phase-shifted topology

Before the magnetic integration, the circuit used two EE cores to wind the transformer and output inductor, separately. An external ring core is used to wind the resonant inductor. Thus, there were three magnetic components in the circuit.

To reduce the size of the magnetic components in the circuit, this paper proposes an integrated magnetic structure, shown in Fig. 2. To obtain lower leakage inductance, the primary- and secondary-side windings are wound around the same core. To prevent saturation due to high dc flux, the output inductor is wound on another core leg, with an air gap. The detailed calculation of the flux density and equivalent output inductance are explained in the next section.

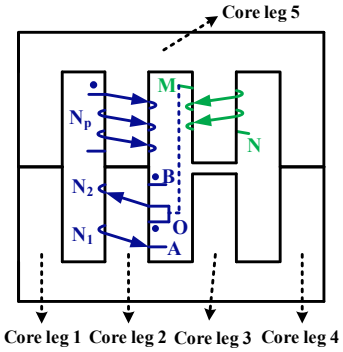

Fig. 2. Magnetic structure after integration

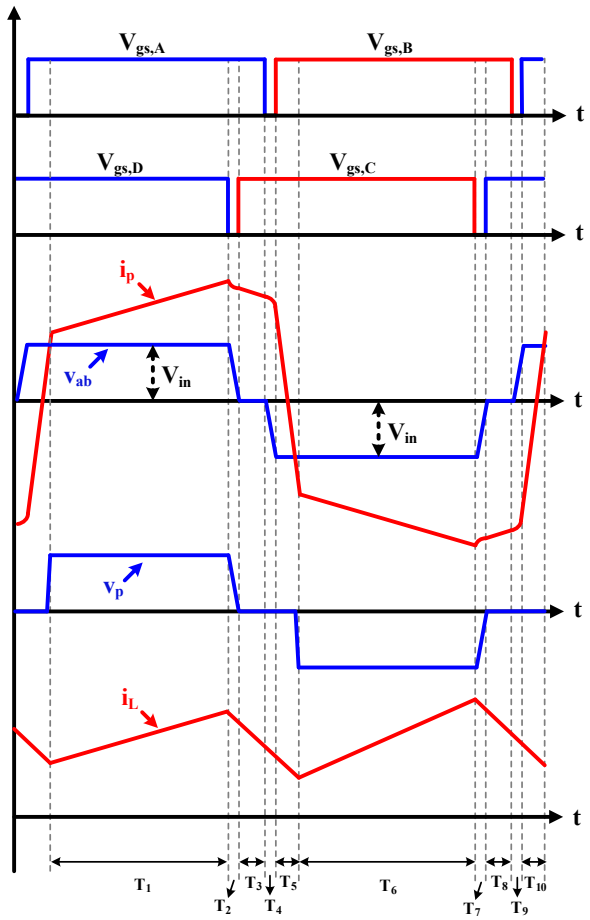

Fig. 3. Waveform of center-tapped full-bridge phased-shifted converter with magnetic integration

The operation waveforms of the center-tapped full-bridge phase-shifted converter with magnetic integration are shown in Fig. 3. The waveforms include resonant inductor current i_p, the voltage of primary-side v_{ab}, the voltage of the primary-side winding v_p, the output inductor current i_{Lo}, and the four switching signals $v_{gs,A}$, $v_{gs,B}$, $v_{gs,C}$, and $v_{gs,D}$. The time interval T_1 to T_{10} is a switching cycle. The analysis of magnetic integration will use these waveforms to derive dc flux, ac flux and equivalent output inductance.

III. Integrated Magnetic Circuit Analysis

The diagram in Fig. 2 can be used to derive the equivalent reluctance model, as shown in Fig. 4. Terms R_1 to R_5 are the equivalent reluctance of core leg 1 to 5, respectively. Terms ϕ_1 to ϕ_5 are the flux of core leg 1 to 5, respectively. The flux ϕ includes dc and ac flux.

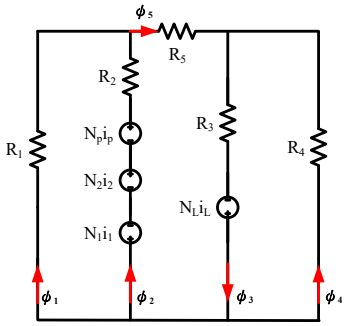

Fig. 4. Equivalent reluctance model

The reluctance equation of the equivalent circuit is

$$R = \frac{l_e}{\mu_r \mu_0 A_e} \tag{1}$$

where l_e is the length of magnetic path, μ_0 is vacuum permeability, μ_r is relative permeability, and A_e is the cross-sectional area of each core leg. The diagram of the core with l_e and A_e are represented in Fig. 5. The following derivation will

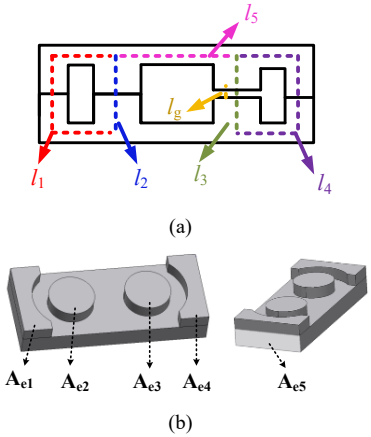

Fig. 5. Diagram of core showing (a) length of magnetic path and (b) cross-sectional area

use these parameters to calculate the dc/ac flux and the equivalent output inductance.

A. DC Flux Analysis

In the integrated magnetic full-bridge phase-shifted circuit, the dc flux is produced by the output inductor. The dc flux equivalent circuit can be drawn as in Fig. 6, where Φ is dc flux and $N_L I_L$ is dc magnetic motive force.

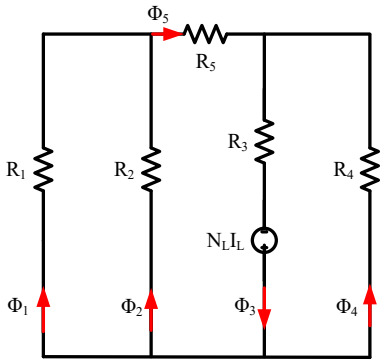

Fig. 6. DC flux equivalent circuit

From Fig. 6, the equivalent total resistance can be derived as following:

$$R_{total} = \frac{\left(\frac{R_1 \times R_2}{R_1 + R_2} + R_5\right) \times R_4}{\frac{R_1 \times R_2}{R_1 + R_2} + R_5 + R_4} + R_3 \tag{2}$$

The dc flux of every core leg can also be derived from Fig. 6, which results in the following equations (3) to (7):

$$\Phi_3 = \frac{N_L \times I_L}{R_{total}} \tag{3}$$

$$\Phi_5 = \Phi_3 \times \frac{R_4}{\frac{R_1 \times R_2}{R_1 + R_2} + R_5 + R_4} \tag{4}$$

$$\Phi_4 = \Phi_3 \times \frac{\frac{R_1 \times R_2}{R_1 + R_2} + R_5}{\frac{R_1 \times R_2}{R_1 + R_2} + R_5 + R_4} \tag{5}$$

$$\Phi_2 = \Phi_3 \times \frac{R_4}{\frac{R_1 \times R_2}{R_1 + R_2} + R_5 + R_4} \times \frac{R_1}{R_1 + R_2} \tag{6}$$

$$\Phi_1 = \Phi_3 \times \frac{R_4}{\frac{R_1 \times R_2}{R_1 + R_2} + R_5 + R_4} \times \frac{R_2}{R_1 + R_2} \tag{7}$$

From the dc flux of every core leg and its equivalent circuit, the third core leg which winds the output inductor has the largest dc flux. Thus, the third core leg needs to be prevented from saturating due to high dc flux. In general, the third core leg has an air gap to solve the problem as mentioned above. The dc flux of every core leg has been derived, the ac flux will be introduced in the next section.

B. AC Flux Analysis

The ac flux can be derived from the equation of Faraday's law which is as follows:

$$v = N \times \frac{d\varphi}{dt} = N \times \dot{\varphi} \tag{8}$$

where v is the voltage on the winding, N is the number of winding turns, φ is the magnitude of ac flux, and $\dot{\varphi}$ is the derivative of the magnitude of ac flux.

To calculate the ac flux, the voltage on the winding must be known. Thus, the result cannot be derived directly using a traditional reluctance model. From (8), the slope of ac flux is positive if the voltage on the winding is positive. On the contrary, the slope of ac flux is negative if the voltage on the winding is negative. This paper will analyze the ac flux of every time interval. To simplify the analysis, this paper ignores the interval of first resonant interval (T_2, T_7) and second resonant interval (T_4, T_9).

1) Stage 1 [T_1]: Energy transfer interval of positive cycle

In this stage, switches Q_A and Q_D (shown in Fig. 1) turn on and the synchronous rectifier Q_E turns on. The waveform for this stage is shown in Fig. 3. Based on the voltage on the winding, the slope of ac flux at the second core leg and third core leg are shown as follows:

$$\dot{\varphi}_{2\_T1} = \frac{V_p(T_1)}{N_p} \tag{9}$$

$$\dot{\varphi}_{3\_T1} = \frac{N_s \times \frac{V_p(T_1)}{N_p} - V_o}{N_L} \tag{10}$$

2) Stage 2 [T_3, T_5]: Free-wheeling interval of positive cycle

When the circuit is at the free-wheeling interval, the synchronous rectifier Q_E and Q_F turn on. For the T_3 and T_5 interval, the waveforms can be seen in Fig. 3. The slope of the ac flux at the second core leg and third core leg during this time interval are as follows:

$$\dot{\varphi}_{2\_T3} = \dot{\varphi}_{2\_T5} = 0 \tag{11}$$

$$\dot{\varphi}_{3\_T3} = \dot{\varphi}_{3\_T5} = \frac{-V_o}{N_L} \tag{12}$$

3) Stage 3 [T_6]: Energy transfer interval of negative cycle

During this time interval, switches Q_B and Q_C turn on and the synchronous rectifier Q_F turns on. The resulting waveforms can be seen in Fig. 3, the slope of the ac flux at the second core leg and third core leg are as follows:

$$\dot{\varphi}_{2\_T6} = \frac{V_p(T_6)}{N_p} \tag{13}$$

$$\dot{\varphi}_{3\_T6} = \frac{-N_s \times \frac{V_p(T_6)}{N_p} - V_o}{N_L} \tag{14}$$

4) Stage 4 [T_8, T_{10}]: Free-wheeling interval of negative cycle

This stage is where the circuit is free-wheeling and the synchronous rectifiers Q_E and Q_F turn on. At the T_8 and T_{10} interval, they have the same equivalent diagram of the winding. The waveforms for these intervals are also shown in Fig. 3. The slope of the ac flux at the second core leg and third core leg during this time interval are as follows:

$$\dot{\varphi}_{2\_T8} = \dot{\varphi}_{2\_T10} = 0 \tag{15}$$

$$\dot{\varphi}_{3\_T8} = \dot{\varphi}_{3\_T10} = \frac{-V_o}{N_L} \tag{16}$$

C. Flux Density Result

The dc/ac flux of each core leg has been derived in Section III.A and III.B. The total flux ϕ is the sum of the dc flux Φ and ac flux φ. Thus, the total flux of the second core leg and third core leg can be determined based on the given equations and an appropriate initial condition. The total flux in the other core legs can be derived using the circuit diagram in Fig. 4 as follows:

$$\phi_5 = \frac{\phi_3 \times R_4 + \phi_2 \times R_1}{R_1 + R_4 + R_5} \tag{17}$$

$$\phi_1 = \phi_5 - \phi_2 \tag{18}$$

$$\phi_4 = \phi_3 - \phi_5 \tag{19}$$

Knowing the total flux of each core leg and the cross-sectional area of the core, the flux density diagram for each core leg is shown in Fig. 7.

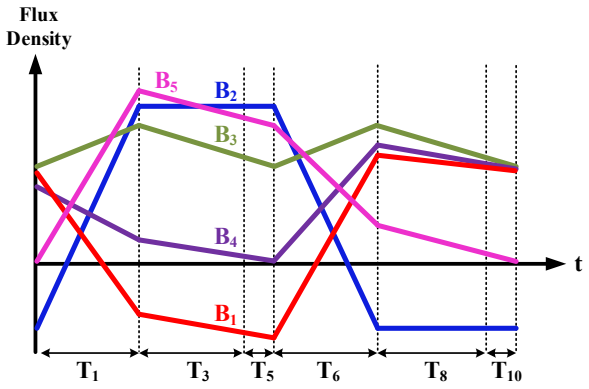

Fig. 7. Flux density of each core leg

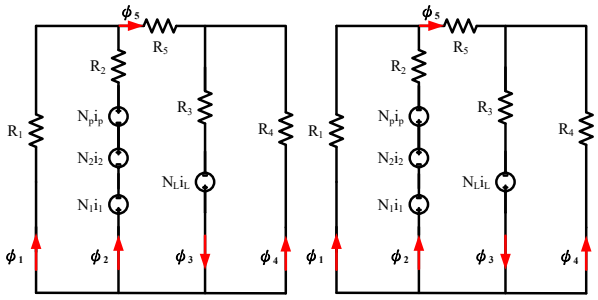

Fig. 8. Equivalent reluctance circuit, (a) Positive cycle, (b) Negative cycle

D. Equivalent Ouput Inductance Analysis

In a full-bridge phase-shifted converter with non-integrated magnetics, the output inductance can be derived from the voltage on the output inductor and expected output current ripple. However, the output inductance cannot be derived in the same way with the integrated magnetic structure. The reason is that the output inductor under the integrated magnetic structure is a coupled inductor. The flux through the third core leg (the output inductor) is influenced by the variation of the transformer's flux. Thus, the equivalent output inductance will be different during each operation interval. To simplify the analysis, this paper ignores the first and second resonant interval. The equivalent reluctance circuit of the positive and negative cycle are shown in Fig. 8.

According to the Fig. 8, superposition is used to derive the relationship between the magnetic motive force and flux of each core leg, using the magnetic permeance to represent these variables. For example, variable P_{32} represents the relationship between the third core leg's magnetic motive force and the second core leg's flux. These variables are as follows:

$$P_{22} = \frac{1}{R_2 + \frac{\left(\frac{R_3R_4}{R_3+R_4} + R_5\right)R_1}{\frac{R_3R_4}{R_3+R_4} + R_5 + R_1}} \tag{20}$$

$$P_{32} = \frac{1}{R_3 + \frac{\left(\frac{R_1R_2}{R_1+R_2} + R_5\right)R_4}{\frac{R_1R_2}{R_1+R_2} + R_5 + R_4}} \frac{R_4}{\frac{R_1R_2}{R_1+R_2} + R_5 + R_4} \frac{R_1}{R_1+R_2} \tag{21}$$

$$P_{23} = \frac{1}{R_2 + \frac{\left(\frac{R_3R_4}{R_3+R_4} + R_5\right)R_1}{\frac{R_3R_4}{R_3+R_4} + R_5 + R_1}} \frac{R_1}{\frac{R_3R_4}{R_3+R_4} + R_5 + R_1} \frac{R_4}{R_3+R_4} \tag{22}$$

$$P_{33} = \frac{1}{R_3 + \frac{\left(\frac{R_1R_2}{R_1+R_2} + R_5\right)R_4}{\frac{R_1R_2}{R_1+R_2} + R_5 + R_4}} \tag{23}$$

In the derivation process, first, derive the total flux of the second and third core leg using (20) to (23). Second, use Faraday's law to derive the relationship between the voltage on the winding and the total flux. After the substitution and calculation, the equivalent output inductance can be derived. The equivalent output inductance during each operation interval is summarized in Table I.

TABLE I. EQIVALENT OUTPUT INDUCTOR

Operation Interval	Equivalent Output Inductance
Stage 1 [T_1] Energy transfer interval of positive cycle	$L_2-\frac{M_1M_2}{L_1}$ / $1-\frac{1}{n}\frac{1}{1-d_{eff}}\frac{M_2}{L_1}$
Stage 2 [T_3, T_5] Free-wheeling interval of positive cycle	$L_2-\frac{M_1M_2}{L_1}$
Stage 3 [T_6] Energy transfer interval of negative cycle	$L_2-\frac{M_1M_2}{L_1}$ / $1+\frac{1}{n}\frac{1}{1-d_{eff}}\frac{M_2}{L_1}$
Stage 4 [T_8, T_{10}] Free-wheeling interval of negative cycle	$L_3-\frac{M_2M_3}{L_1}$

The variables L_1, L_2, L_3, M_1, M_2, and M_3 represent are defined as follows:

$$L_1 = P_{22}N_p^{\,2} \tag{24}$$

$$L_2 = N_L\left(P_{33}N_L - P_{23}N_s\right) \tag{25}$$

$$L_3 = N_L \times \left(P_{33}N_L + P_{23}N_s\right) \tag{26}$$

$$M_1 = N_p\left(P_{32}N_L - P_{22}N_s\right) \tag{27}$$

$$M_2 = N_L N_p P_{23} \tag{28}$$

$$M_3 = N_p \times \left(P_{32}N_L + P_{22}N_s\right) \tag{29}$$

IV. EXPERIMENT RESULT

The integrated magnetics of the full-bridge phase-shifted converter is developed with input voltage at 380 V, output voltage at 12 V, output current at 41.6 A, and switching frequency at 100 kHz. The primary-side winding is 14 turns and the secondary-side winding is 1 turn. For the lagging leg to achieve ZVS, the resonant inductor must be at least 20 μH.

In this paper, the resonant inductor is replaced by the transformer's leakage inductor, achieved by adjusting the distance between the primary-side winding and secondary-side winding. The distance between two windings was chosen as 10 mm, such that the leakage inductance is 22 μH.

The output inductor winding is 3 turns which has ±7A output ripple current. From the previous derivation, the flux density of the core under full load conditions is shown in Fig. 9. Variables B_1 to B_5 are the flux density of core legs 1 to 5, respectively. The unit of flux density is tesla (T). In Fig. 9, the maximum flux density of the core is 0.18 T. The derivation result can be used to check whether or not the flux density exceeds the maximum saturation flux density of the core.

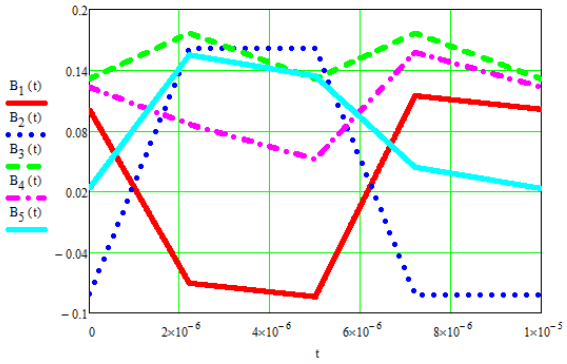

Fig. 9. Flux density of integrated magnetic core

The integrated magnetic circuit's primary-side current i_p and output inductor current i_{Lo} waveform under full-load condition are shown in Fig. 10. The waveforms of the output inductor current ripple are shown in Fig. 11. One switching cycle goes from interval 1 to interval 4. From the waveform, the equivalent output inductance can be derived from the slope of the current ripple during each operation interval. The comparison between the theoretical and experimental equivalent output inductance is give in Table II, where the experiments results are similar to the theorem derivation.

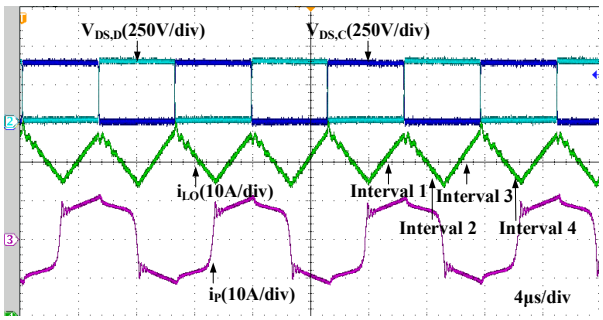

($v_{DS,C}$/$v_{DS,D}$：250 V/div、i_p：5 A/div、i_{Lo}：10 A/div、Time：4 μs/div)

Fig. 10. Key waveforms under full load conditions

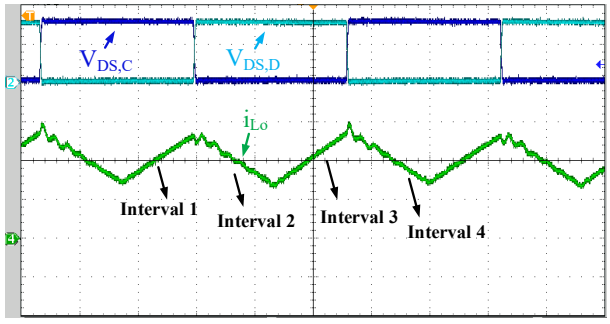

Fig. 11. Detailed waveform of the output current ripple

The integrated magnetic core and the center-tapped full-bridge phase-shifted circuit is shown in Fig. 12. The length, width, and height are 16 cm, 11 cm, and 3 cm, respectively.

(a)

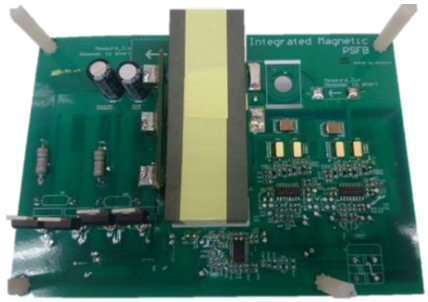

(b)

Fig. 12. Integrated magnetic (a) core structure and (b) circuit board

TABLE II. THEORTICAL AND EXPERIMENTAL COMPARISON

Operation Interval	Theorem Result	Actual Result
Interval 1: Energy transfer interval of positive cycle	2.7 μH	2.904 μH
Interval 2 : Free-wheeling interval of positive cycle	2.599 μH	2.825 μH
Interval 3 : Energy transfer interval of negative cycle	2.505 μH	2.75 μH
Interval 4 : Free-wheeling interval of negative cycle	2.599 μH	2.825 μH

The efficiency curve of the integrated magnetic circuit is shown in Fig. 15. The circuit achieves efficiency of about 91% at half load and about 90% at full load.

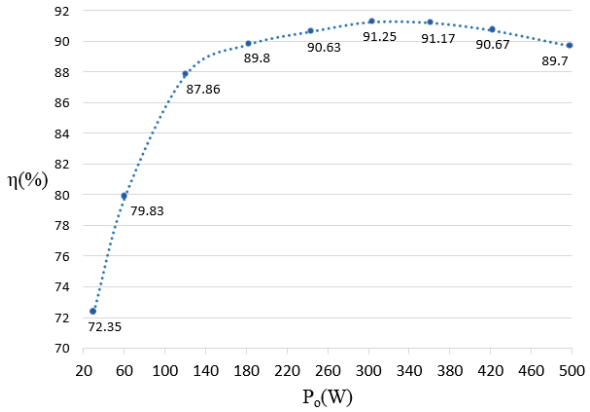

Fig. 15. Efficiency curve of integrated magnetic circuit

V. CONCLUSION

This paper proposes a new magnetic integration technique for a center-tapped full-bridge phase-shifted converter. Using this technique to integrate all the magnetic components into one core. The dc and ac flux during each operation interval was analyzed to derive the flux density, which is used to prevent saturation of the core. The equivalent output inductance was derived based on the output ripple current. The resonant inductor in the traditional circuit is replaced by adjusting the distance between the primary-side winding and secondary-side winding. Finally, a 500-W prototype center-tapped full-bridge phase-shifted converter, operating with 380-V input voltage and 12-V output voltage was implemented to prove the feasibility of the magnetic integration technique.

ACKNOWLEDGMENT

This research was supported in part by the National Science Council of Taiwan under Grant MOST 106-2221-E-197-015-, and the Basic Science Research Program through the National Research Foundation of Korea (NRF) funded by the Ministry of Education (2016R1D1A1B03931573).

REFERENCES

[1] J. G. Cho, J. A. Sabate, and F. C. Lee, “Novel full bridge zero-voltage-transition PWM DC/DC converter for high power applications,” IEEE APEC, 1994, pp.143-149.

[2] C. M. Wang, “A new family of zero-current-switching (ZCS) PWM converter,” IEEE Transactions on Power Electronics, vol. 52, no. 4, pp. 1117-1125, Aug. 2005.

[3] X. Ruan and F. Liu, “An improved ZVS PWM full-bridge converter with clamping diodes,” IEEE Transactions on Power Electronics, 2004, pp. 1476-1481.

[4] W. Chen, X. Ruan, and R. Zhang, “A novel zero-voltage-switching PWM full bridge converter,” IEEE Transactions on Power Electronics, vol. 23, no. 2, pp. 793-801, Mar. 2008.

[5] Z. Emami, M. Nikpendar, N. Shafiei, and S. R. Motahari, “Leading and lagging-legs power loss analysis in ZVS phase-shift full bridge converter,” Proc. PEDSTC, 2011, pp. 632-637.

[6] H. Lei, J. Guo, X. Jing, N. Mi, R. Chung, and S. Luo, “Design considerations for secondary side synchronous rectifier MOSFETs in phase shifted full bridge converter,” IEEE APEC, 2013, pp. 526-531.

[7] S. Lei, Z. J. Su, and Y. T. Chang, “Design and optimization of parallel DC-DC system based on current-driven phase shift full bridge converter,” IEEE APEC, 2014, pp. 2048-2053.

[8] P. Wong, Q. Wu, P. Xu, B. Yang, and F. C. Lee, “Investigating coupling inductors in the interleaving QSW VRM,” IEEE APEC, 2000, pp. 973-978.

[9] P. L. Wong, F. C. Lee, X. Jia, and D. V. Wyk, “A novel modeling concept for multi-coupling core structures”, IEEE APEC, 2001.

[10] P. Xu and F. C. Lee, “Design of high-input voltage regulator modules with a novel integrated magnetics,” IEEE APEC, 2001, pp. 112-115.

[11] R. Chen, F. Canales, B. Yang, P. Barbosa, J. D. van Wyk, and F. C. Lee, “Integration of electromagnetic passive components in DPS front-end DC/DC converter-a comparative study of different integration steps,” Proc. IEEE APEC, 2003, pp. 1137-1142.

[12] A. A. Aboulnaga and A. Emadi, “Simplified simulation and modeling technique for integrated magnetic components in power electronic converters,” in Proc. 26th Annu. INTELEC, 2004, pp. 725-730.\

[13] W. Chen, G. Hua, D. Sable, and F. C. Lee, “Design of high efficiency, low profile low voltage converter with integrated magnetics,” IEEE APEC, 1997, pp. 15-21.

[14] A. Pietkiewicz and D. Tollik, “Coupled-inductor current-doubler topology in phase-shifted full-bridge dc–dc converter,” Proc. IEEE INTELEC, 1998, pp. 41-48.

[15] P. Xu, Q. Wu, P. L. Wong, and F. C. Lee, “A novel integrated current doubler rectifier,” IEEE APEC, 2000, pp. 735-740.

[16] P. Xu, M. Ye, and F. C. Lee, “Single magnetic push-pull forward converter featuring built-in input filter and coupled inductor current doubler for 48V VRM”, IEEE APEC, 2002, pp. 843-849.

[17] P. Xu, M. Ye, P. Wong, and F. C. Lee, “Design of 48-V voltage regulator modules with a novel integrated magnetics,” IEEE Trans. Power Electron., vol. 17, no. 6, pp. 990-998, Nov. 2002.

[18] J. Sun, K. F. Webb, and V. Mehrotra, “Integrated magnetics for current doubler rectifiers,” IEEE Trans. Power Electron., vol. 19, no. 3, pp. 582-590, Nov. 2004.

[19] H. Zhou, T. X. Wu, I. Batarseh, and K. D. T. Ngo, “Comparative investigation on different topologies of integrated magnetic structures for current-doubler rectifier,” IEEE PESC, 2007, pp. 337-342.

[20] P. Meng, X. Wu, C. Zhao and Z. Qian, "Integrated Magnetics ZVS Full-Bridge Converter with Phase-Shift control," IEEE APEC, Washington, DC, 2009, pp. 1434-1439.

[21] L. U. Zengyi, Y. Haijun, and Z. Alpha, “New magnetic integration of full-wave rectifier with center-tapped transformer” IEEE Trans. Power Electron, 2014.